ORIGINAL ARTICLE

Absorbing aerosol decreases cloud cover in cloud-resolving simulations over Germany

F. Senf[1] | **J. Quaas**[2] | **I. Tegen**[1]

[1]Leibniz Institute for Tropospheric Research, Leipzig, Germany.

[2]Leipzig Institute for Meteorology, Universität Leipzig, Leipzig, Germany.

Correspondence
Fabian Senf, Leibniz Institute for Tropospheric Research, Leipzig, Germany
Email: senf@tropos.de

Funding information
The study was perform in the frame of the german-wide High Definition Clouds and Precipitation for advancing Climate Prediction (HD(CP)^2) project funded by the BMBF (German Ministry for Education and Research). FS and IT acknowledge funding under grant 01LK1503F; JQ acknowledges the HD(CP)^2 grant 01LK1503A and funding from the EU Horizon 2020 project CONSTRAIN (GA 820829).

Aerosol can affect clouds in various ways. Beside the microphysical impact of aerosol particles on cloud formation, the interference of aerosol with atmospheric radiation leads to changes in local heating, surface fluxes and thus meso-scale circulations all of which may also modify clouds. Rather little is known about these so-called semi-direct effects in realistic settings - a reason, why this study investigates the impact of absorbing aerosol particles on cloud and radiation fields over Germany. Using advanced high-resolution simulations with grid spacings of 312 and 625 m, numerical experiments with different aerosol optical properties are contrasted using purely-scattering aerosol as control case and realistic absorbing aerosol as perturbation. The combined effect of surface dimming and atmospheric heating induces positive temperature and negative moisture anomalies between 800 and 900 hPa impacting low-level cloud formation. Decreased relative humidity as well as increased atmospheric stability below clouds lead to a reduction of low-level cloud cover, liquid water path and precipitation. It is further found that direct and semi-direct effects of absorbing aerosol forcing have similar magnitudes and equally contribute to a reduction of net radiation at the top of the atmosphere.

KEYWORDS
Absorbing Aerosol, Semi-Direct Effects, High-Resolution

1 | INTRODUCTION

Absorbing aerosol plays an important role in Earth's climate system and contributes to the human impact on climate (Grassl, 1975; Bond et al., 2013; Boucher et al., 2013). Absorbing aerosol such as black carbon in soot absorbs incoming solar radiation (Ramanathan et al., 2001) changing the energy content of the atmosphere. It leads to modifications of the stability in the atmospheric boundary layer and free troposphere and thus to perturbations in the thermal structure of the atmosphere influencing cloud formation and maintenance (Ackerman et al., 2000; Koch and Del Genio, 2010). Aerosol also reduces the downwelling solar radiation at the surface which has been referred as surface dimming (Liepert, 2002; Feingold et al., 2005; Ramanathan and Carmichael, 2008; Wild, 2009). Over the land surface, this dimming by absorbing aerosols can lead to a substantial reduction in surface latent and sensible heat fluxes. Anticipated changes in surface fluxes were found to be sufficiently large to explain a substantially reduction of cloudiness due to smoke in the Amazonian rain forest (Feingold et al., 2005). Moreover, surface dimming by absorbing aerosol, e.g. from anthropogenic pollution, can decrease precipitation and thus impact water availability in the East Asian summer monsoon by cooling the land surface (Ramanathan and Carmichael, 2008; Persad et al., 2017). Taken together, the changes in atmospheric stability and reduction in surface fluxes could act to significantly modify the fraction of clouds, especially that of low-level clouds coupled to boundary layer processes. The actual changes in the planetary albedo and consequently in the Earth's energy balance depend on several factors, including the altitude of the aerosol layers relative to the clouds and the impacted cloud type (Koch and Del Genio, 2010; Ming et al., 2010). The impact of absorbing aerosol on clouds was initially called "semi-direct effect" (Hansen et al., 1997; Lohmann and Feichter, 2001) and is in more recent literature in a more general perception considered part of the rapid adjustments to aerosol-radiation interactions (Myhre et al., 2013b; Sherwood et al., 2015).

In the latest climate assessments, a negative value is assigned to the net global effective radiative forcing of aerosol-radiation interactions - but it has been also made clear that the current scientific understanding is low in terms of agreement and confidence level (Flato et al., 2014). It has been further stated that "while there is robust evidence for the existence of rapid adjustment of clouds in response to aerosol absorption, these effects are multiple and not well represented in climate models, leading to large uncertainty" (Boucher et al., 2013, see p. 573). Reasons for the disagreements between global models and regional high resolution simulations are not always understood, making it difficult to infer a consistent picture (Bond et al., 2013). Studies examining marine clouds impacted by atmospheric heating due to absorbing aerosol on a regional scale have found both reductions in cloudiness (a positive forcing) (Ackerman et al., 2000) but also increases and thickening (a negative forcing) (Wilcox, 2012; Gordon et al., 2018). Over land, a reduction of surface latent and sensible heat fluxes due the aerosol-induced dimming must be considered as an additional effect that does not play a particular role for marine clouds. Realistic convection-permitting modelling studies could show that the cooling of the land surface and the simultaneous atmospheric heating aloft causes substantial adjustments in vertical temperature stratification and is typically responsible for a suppression of convective clouds and precipitation (Huang et al., 2016; Wu et al., 2011). Thus, for semi-direct effects of absorbing aerosol, cloud cover could increase or decrease, depending on region and weather conditions. Moreover, it has been discussed that aerosol–radiation interactions and aerosol–cloud interactions of biomass burning aerosol over land show opposite signs and thus compensate each other (Liu et al., 2020; Lin et al., 2021).

In modelling studies, the net effect on radiation is usually inferred from two sets of simulations — one with and one without conditions perturbed by pollution aerosol (Bond et al., 2013). Here, this strategy has been applied to

cloud-resolving ICOsahedral Non-hydrostatic Large Eddy Model (ICON-LEM) simulations to investigate the impact of aerosol absorption over Germany. ICON-LEM is run with hectometre-scale horizontal grid spacings in a limited-domain setup with different aerosol optical properties. The chosen high-resolution setup allows for realistic semi-direct responses of cloud fields and cloud-scale circulations to aerosol-induced changes in atmospheric heating and surface fluxes. Moreover, the atmospheric part of ICON is coupled to a sophisticated surface model to further increase the realism of the atmosphere-surface interaction, and the model is run using realistic initial and boundary conditions in numerical-weather-prediction-type mode. The outlined research bridges the gap between currently published studies on LES (large eddy simulation) modelling with idealised or semi-idealised setups (typically applied to investigate marine clouds) and convective-permitting modelling applied for more realistic configurations e.g. including the response of land surface modules. From a general perspective, our research further contributes to the scientific understanding of regional rapid adjustments to aerosol-radiation interactions which is important for a further reduction of the uncertainty of aerosol- and cloud-related processes in a changing climate (Flato et al., 2014; Bellouin et al., 2020).

The rest of the paper is structured as follows: We explain the ICON model setup, the conducted sensitivity experiments and the general framework of our object-based analysis of liquid water path (LWP) fields in Section 2. The main results are presented in Section 3 which considers the changes in atmospheric stability and the radiative forcing due to aerosol perturbations as well as responses of LWP and precipitation. We provide a discussion of our results in Section 4 and close with a summary in Section 5.

2 | DATA AND METHODS

2.1 | ICON Model

The ICON (ICOsahedral Non-hydrostatic) modelling framework was jointly developed by the German Meteorological Service and the Max Planck Institute for Meteorology (Zängl et al., 2014). For our study, we apply the ICON-LEM configuration that was specifically adjusted for high-resolution simulations (Dipankar et al., 2015). This setup was extensively evaluated against a comprehensive set of observations (Heinze et al., 2017). In addition, Stevens et al. (2020) showed that the general representation of clouds and many other important aspects of the structure of cloud fields are considerably improved, compared to coarse-resolved simulations, when hectometre-scale simulations are afforded despite their significant computational demand.

The ICON dynamical core solves the fully compressible non-hydrostatic equations of motion on a triangular grid. The discretization of the air and tracer transport is such that mass of air and its constituents is conserved (Zängl et al., 2014). In the vertical, ICON is discretized using a height-based terrain-following coordinate system. The ICON-LEM physics package includes sophisticated parameterisations for land surface processes (TERRA model, Heise et al., 2006), three-dimensional diagnostic sub-grid turbulence (3-dim. Smagorinsky closure), cloud microphysical processes, and radiative transfer. Cloud condensate is separated into six hydrometeor categories (cloud droplets and rain for liquid condensate; cloud ice, graupel, snow and hail for frozen condensate). For each category, number and mass concentrations are forecast using the two-moment scheme after Seifert and Beheng (2005). Radiative transfer is calculated by the global model version of the Rapid Radiation Transfer Model, RRTMG (Mlawer et al., 1997). RRTMG uses 14 bands in the shortwave and 16 bands in the longwave.

In the ICON-LEM version, applied in the current study, aerosol-radiation interactions (ARI) are considered independently of aerosol-cloud interactions (ACI). For ARI, temporally constant aerosol optical properties are input as external parameters, whereas for ACI, the model digests prescribed cloud condensation nuclei concentrations follow-

ing Costa-Surós et al. (2020). The latter is not related to the aerosol-optical properties data. However, this apparently inconsistent formulation is used here to its advantage. Aerosol perturbations can be formulated such that only direct and semi-direct effects of aerosol forcing are considered, whereas indirect effects via cloud microphysical adjustments are excluded. In any case, aerosol is neither interactively transported with the simulated flow nor processed by simulated clouds or precipitation. This means that a potential buffering of the radiative effects by thermodynamical or cloud microphysical feedbacks as for instance outlined by Yamaguchi et al. (2015) for the interaction between smoke and marine clouds is not included in our study.

For ARI, aerosol optical properties are taken as static, external data (no interactivity) from the Global Aerosol Climatology Project (GASP, Tegen et al., 1997) which provides data for monthly-mean aerosol optical properties for a representative aerosol mixture. The horizontal resolution of GASP aerosol optical depth (AOD) data is $4^\circ \times 5^\circ$ and thus very coarse leading to rather similar conditions across the whole domain and very weak horizontal AOD gradients. AOD at 550 nm is input for different GASP classes and subsequently mapped onto four prescribed ICON aerosol classes. Taking all together, the total domain-average AOD is around 0.21 at 550 nm (minimum and maximum AOD values reach 0.16 and 0.25, respectively). The four ICON aerosol classes represent the types "continental", "marine", "dust" and "urban" which provide respective contributions of 67%, 0.8%, 19% and 14% to the total AOD. When weighted by the incoming radiation fluxes in the respective solar bands, the broad-band single scattering albedo of the aerosol mixture is 0.89, i.e. 11% of the extinct solar flux is absorbed. The broadband absorption AOD of the mixture is 0.017. Continental aerosol contributes half, dust and urban aerosol each around a quarter to the total absorption AOD. A simple exponential decay with altitude is assumed for the vertical profiles of aerosol optical properties which is generally consistent with findings from comprehensive air quality model simulations (Curci et al., 2019). For ACI, completely different aerosol distributions are ingested into the ICON model. The methodology follows the one described by Costa-Surós et al. (2020) (denoted there as "C2R" run). Three-dimensional distributions of cloud condensation nuclei (CCN) are pre-calculated after Genz et al. (2020) and provided to ICON as external data. Cloud-microphysical adjustments only care about these prescribed CCN fields, but are independent of perturbations in aerosol-radiation interactions.

2.2 | Experiment Setup

The simulations are performed in a limited-area setup covering Germany with a rectangular domain extending from 4.5 to 14.5°E and from 47.6 to 54.6°N. All physical parameterizations are configured in a similar way as described in Heinze et al. (2017). In addition to the above mentioned radiation and grid-scale microphysics scheme, cloud cover is parametrized by an all-or-nothing scheme that does not account for humidity fluctuations at subgrid scales. Turbulent mixing is parametrized by a three-dimensional, local and diagnostic Smagorinsky scheme applied on prognostic winds, potential temperature, specific humidity and specific cloud liquid water content with modifications to account for thermal stratification (see Dipankar et al., 2015). Two high-resolution ICON-LEM configurations with respective horizontal grid spacings of 625 m and 312 m are coupled using one-way nesting. The outer nest is initialised at 0z with initial conditions and subsequently driven by realistic lateral boundary conditions obtained from hourly updated analysis of the COSMO-DE model (Baldauf et al., 2011). The initialization also includes soil properties. In the vertical, the same configuration is used for both nests with a total number of 150 vertical levels, with a grid stretching towards the model top at 21 km and with a minimal layer thickness of 20 m near the surface (Heinze et al., 2017). The simulations in the two different nests allow to test for horizontal resolution sensitivities and build a minimal simulation ensemble. In the case, where the sensitivity experiments described below differ at two resolutions qualitatively it is believed that the simulated response can not be attributed to aerosol perturbations. The chaotic and turbulent nature

of the atmospheric motion supposedly governs the divergent evolution of the model results in that case.

Due to the high computational cost, we only consider 24-hour forecasts for one single day during mid-latitude spring, i.e. 2 May 2013. This day falls into a period of intensive observations during the High Definition Clouds and Precipitation for Climate Prediction (HD(CP) ^{2}) Observational Prototype Experiment (HOPE; Macke et al., 2017). The cloud scenery is characterised by a complex mixture of stratiform and convective cloud types on that day on which the considered region was dominated by a high-pressure system (see e.g. Figures 1 and 9 in Costa-Surós et al., 2020). For a more detailed description of the weather situation and supplementary observations, the reader is referred to Heinze et al. (2017) and Costa-Surós et al. (2020).

Two distinct model experiments were conducted: In the first experiment, the complete aerosol-radiation interaction is considered as described above. Therefore, aerosol optical properties after Tegen et al. (1997) are included into radiative transfer calculations. Simplified aerosol profiles are specified such that the largest amount of aerosol is found in the planetary boundary layer. A realistic mixture of aerosol types with different contributions to scattering and absorption is taken into account. This experiment is abbreviated with *"absorbing"* in the following to clarify that it represents the effects of aerosol absorption. However, we like to emphasise that the "absorbing" experiment does not exclude the effects of aerosol scattering. In the second experiment, absorption coefficients for all aerosol species are set to zero, but keeping scattering properties at the predefined values. Hence, aerosols impact shortwave and longwave radiation flux calculations (RRTMG) only via scattering. This experiment is abbreviated with *"scattering"* in the following. Broadband AODs decrease from 0.163 in the "absorbing" experiment to 0.146 in the "scattering" experiment. Thus using the Beer-Lambert law for a simple estimate (Petty, 2006), the atmospheric transmittance would be reduced by 1.7% in the "absorbing" experiment, thus about one to two percent less solar radiation would reach the surface.

For subsequent analysis, all ICON output fields were regridded onto a regular longitude-latitude grid with an average grid spacing of 5 km. Using the difference of the two experiments, the direct and semi-direct effects of aerosol absorption can be inferred. The “scattering” experiment with no aerosol absorption is taken as reference in the following. In that way, changes in cloud cover and other atmospheric variables can be attributed to the added aerosol absorption. In other words, we can answer the question of how much the atmosphere including its condensate is changed by increasing aerosol absorption to current levels.

2.3 | Object-based Analysis

In combination with traditional statistics like domain average and standard deviation, we apply an object-based analysis to our simulations. The underlying assumption is that the additional information from the object properties facilitates the physical interpretation of the results (Gilleland et al., 2009; Ebert et al., 2013). If, for instance, the liquid water path (LWP) field is composed of a high number of small, but intense objects, we interpret the cloud scenery as convective situation. In contrast, if large and more homogeneous LWP objects appear then the cloud scenery is composed of more stratiform clouds.

For the derivation of objects, a threshold-based segmentation is applied (see e.g. Rempel et al., 2017; Senf et al., 2018). In this methodology, a predefined threshold is used to mask a two-dimensional atmospheric field, e.g. LWP. In the resulting binary mask, field values larger than the threshold correspond to the areas of interest which form the objects. Contiguous regions which are connected across edges (4-connectivity) get a unique label. No smoothing of the input field and no size-related filtering of the objects is applied. Finally, object properties are derived as sum or mean over all grid boxes sharing the same object label.

In a further analysis step, we apply a technique that intends to match objects between the "scattering" and the

"absorbing" experiment. This allows to make statements about which objects exist in both simulations and how they have changed, and additionally to identify newly formed objects. Matching objects from different sources is a typical task for object-based forecast verification (e.g. Davis et al., 2009). In our case, we utilise the fact that the difference between both simulation experiments is caused by small perturbations and thus the simulations remain rather close to each other. We define objects that overlap between the two experiments as matching objects. For this calculation, the object labels of one experiment (e.g. "scattering") are mapped onto the binary mask of the other experiment (e.g. "absorbing"). Areas of interest that are not assigned to a label by this mapping are filled with a region growing method, also called watershed segmentation (see Senf et al., 2018; Heikenfeld et al., 2019, for an extended description). This second segmentation calculation stabilises the analysis to a considerable degree and makes it less sensitive to subsequent splits and merges due to filament connections (see Weniger and Friederichs, 2016, for a critical discussion of sensitivities). Slightly different statistics result from the two possible matching options, i.e. matching "scattering" objects to "absorbing" objects" and vice versa. We average the two options to arrive at the final statistics.

3 | RESULTS

3.1 | Atmospheric Stability Changes due to Aerosol Perturbations

We start with the direct response of radiative fluxes to aerosol perturbations which then lead to changes in atmospheric stability. Figure 1a provides domain-average profiles of radiative heating rates derived in areas that are defined as clear-sky in both ICON experiments ("absorbing" and "scattering"). In general, longwave radiation fluxes only warm lowermost atmospheric layers and thereby transfer energy from the Earth surface to the atmosphere by a rate of about 5 Kelvin per day. The rest of the atmosphere is cooled by emission of longwave radiation into space. The absorption of shortwave radiation by gases induces a warming throughout the atmosphere by a few Kelvin per day. The warming increases towards the surface reaching values similar to the longwave heating. If aerosol absorption is taken into account, the shortwave heating is increased by 1 to 1.5 Kelvin per day (see Fig. 1b). The difference in shortwave heating increases towards the surface which brings an additional energy input into the planetary boundary layer below the free troposphere. The functional shape of the heating difference is solely determined by the aerosol concentration profile which was specified as a simple exponential decay with height. Thus, the maximum heating rate difference in the domain lies below any clouds. Different heating rate profiles could be realised depending on where the maximum concentration of absorbing aerosol is found. As reviewed by Koch and Del Genio (2010), knowledge about the location of the aerosol layer relative to the clouds is crucial for the understanding how cloud development and precipitation formation is impacted. Also longwave heating is modified by absorbing aerosol, but to a smaller amount compared to shortwave heating. The additional aerosol absorption in the longwave part of the spectrum leads to smaller vertical gradients in the longwave fluxes and to an increased longwave emissivity of the lower atmosphere, therefore inducing a cooling anomaly. Although the longwave effects are of second order during daytime compared to shortwave heating, they may become relatively more important overnight.

The impact of clouds on the shortwave radiative heating differences is shown in Fig. 1c. For this analysis, the differences of cloudy heating profiles have been subtracted from the differences in clear-sky heating profiles. Furthermore, broken-cloud and overcast areas have been identified based on cloud cover (see figure caption for the definition). Below approximately 850 hPa, clouds reduce the heating due to absorbing aerosol and thus provide a cooling contribution relative to the clear-sky heating. This is just due to the fact that less radiative energy is available for aerosol absorption below clouds. Overcast clouds have an higher average albedo than broken clouds. The amount of reflected radiation is increased for overcast clouds making more radiation available for absorption in the upwelling

branch above clouds. Thus, in this way, a large cloud deck can increase the top-of-the-atmosphere direct aerosol radiative effect (Chand et al., 2009). Overall, the shown shortwave heating pattern, with a relative cooling below and a relative heating above clouds, leads to a slight stabilisation of the atmosphere relative to the clear-sky changes.

The average response of the atmosphere due to the applied aerosol absorption perturbation is shown in Fig. 2. Besides the few lowest layers close to the surface, the simulated atmosphere is stably stratified on average. In both, the 312 m and the 625 m model setups, the absorption-induced anomalies of mean thermodynamic quantities are very similar. This provides a hint that the analysed response is caused more likely by aerosol changes than by changes in the (possibly chaotic) weather evolution. In Fig. 2a, the largest change in domain-average temperature is found slightly below 850 hPa within the low-level cloud layer. The temperature peak has its origin in the superposition of two opposite effects. First, the positive shortwave heating anomaly (see Fig. 1b) forces a positive temperature anomaly that increases towards the surface. Secondly, as the absorbing aerosol hinders shortwave radiation from reaching the Earth's surface, a so-called dimming effect occurs. This has the consequence that less solar energy is added to the surface energy budget which consequently lowers the surface temperature and the amount of the upwelling latent and sensible heat fluxes. Thus, the boundary-layer circulations transport less energy away from the surface and a negative temperature perturbation develops that counteracts the effects of increased local shortwave heating. The profile of the temperature anomaly indicates that the combined action of surface dimming and atmospheric heating increases atmospheric stability below the low-level cloud layer. Absorption-induced atmospheric heating is however the dominant effect above the cloud layer and causes a reduction in atmospheric stability.

Even though latent heat fluxes are reduced due to surface dimming, a positive humidity anomaly develops near the surface (Fig. 2b). Surprisingly, the humidity anomaly at the surface is so high that temperature and humidity anomalies contribute equally to the change of the atmospheric enthalpy (around 25 $\mathrm{J\,kg^{-1}}$) and also that the relative humidity (RH) at the surface is not changed at all, i.e. $\Delta\mathrm{RH} = 0$ (not shown). At higher altitudes, the humidity anomaly has a negative peak in the centre of the cloud layer. With higher temperature and lower humidity between 900 and 800 hPa, the liquid cloud field experiences a negative impact. In the domain average, the cloud coverage is reduced with the largest reduction of -1% peaking at around 900 hPa (see Fig. 2c). In the mid-levels between 800 and 500 hPa, a small positive humidity anomaly is found. However, the impact of the aerosol perturbation is less clear and also much more uncertain for mid-level and high clouds.

As stated in Section 2.2 and further discussed by Heinze et al. (2017), the simulated cloud scenery is composed of a mixture of stratiform and convective clouds. The western half of the domain is more convectively characterised, whereas the large, more stratiform cloud decks exist in the eastern part of the domain. In order to enable a separation between the responses of convective and stratiform regimes to aerosol perturbations, Fig. 3 shows profiles of cloud water and cloud-related fluxes individually averaged for a western and for an eastern sub-domain. A further distinction of cloud regimes is carried out at in the next section based on lower tropospheric stability. Here, it can be seen that specific cloud water content q_c maximises around 850 hPa (Fig. 3a) similar to cloud cover. Significantly more cloud water content is found in the eastern sub-domain, i.e. in the stratiform cloud regime. The cloud-water anomalies peak slightly below the maximum of the absolute values of the reference case with much higher magnitudes in the eastern sub-domain, but similar relative reductions of around $-10\,\%$ in the Δq_c-minimum. Thus, in a relative sense, the analysed cloud-water responses are similar in convective and in stratiform cloud regimes. The distinction between convective and stratiform cloud dynamics can also be identified based on Fig. 3b in which the average liquid water flux reaches much higher up in the convective regime. The flux anomaly shows increasingly negative values from the surface up to around 900 hPa. From this levels upwards, resolution sensitivity dominates the water-flux anomalies, especially in the convectively characterised eastern part, and even the sign of the water-flux anomaly seems to be uncertain. Finally, upward-directed flux of vertical momentum is presented in Fig. 3c as measure of boundary-layer

and cloud-related circulations. This quantity peaks below the cloud base around 950 hPa and shows a very high sensitivity to horizontal resolution. As discussed in Heinze et al. (2017), the grid spacing of a few hectometres is not sufficient to resolve the full spectrum of boundary-layer and cloud-related circulations, thus vertical motions remain partly under-resolved even in our high-resolution setup. The momentum-flux anomalies show a consistent reduction of vertical motion below the cloud base which is more pronounced in the convectively characterised eastern part. This makes clear that the previously discussed stabilisation of the lower atmosphere weakens the development of circulations and thus mixing and vertical water transport in the planetary boundary layer.

3.2 | Assessment of Radiative Forcing

In the following, we assess how changes in cloud cover are linked to changes in radiative fluxes at the surface and at the top of the atmosphere. The temporal evolution of low-level cloud cover is shown in Fig. 4a. A negative cloud cover anomaly already develops at night, i.e. in the absence of sunlight. The effect could be potentially attributed to the increased longwave opacity of the atmosphere due to additional aerosol absorption in the longwave. Due to this, low-level clouds would be slightly less efficient to cool at night via longwave emission from cloud tops. This would lead to a small positive temperature anomaly within the low-level cloud layer causing evaporation of liquid cloud condensate and therefore the initial cloud cover starts to decrease. After sunrise, a different regime sets in and cloud cover is depleted much more efficiently. As already described earlier, the direct shortwave heating due to absorbing aerosol induces a positive temperature anomaly and a negative humidity anomaly that both negatively influence liquid cloud amount. In addition, reduced surface fluxes due to surface dimming cause an increase in atmospheric stability of the boundary layer which partially hinders convective cloud development. The net shortwave radiation that reaches the Earth's surface is reduced by the impact of absorbing aerosol (see Fig. 4b). The peak reduction of net shortwave radiation around $-8\,\mathrm{W\,m^{-2}}$ occurs between 8 and 9z. In this time and earlier, the reduction in net shortwave radiation is mainly caused by the dimming effect of absorbing aerosol. The relative increase in net shortwave radiation around local noon (11z) comes from the change in direct solar radiation at the surface which increases because less low-level clouds reflect shortwave radiation back to space before it reaches the surface. The spatial distributions of cloud cover and shortwave radiation anomalies are visualised in Fig. 4c-e for illustration. The large and more stratiform cloud deck in the east of the domain remains rather stable and mainly looses areal extent at the edges. More irregular patterns of cloud cover change are found in the more convective, western part of the domain. More generally, we could think of the boundary layer - cloud coupling as a buffered system which tries to minimise the loss of incoming energy by reducing the amount of low-level clouds which would otherwise shade the surface in addition to the aerosol-induced surface dimming.

As seen in the visualised maps (Fig. 4), cloud cover and radiative fluxes seem to respond differently to applied aerosol perturbations in the convective and in the stratiform regions. For a statistical assessment of this aspect that goes beyond the separation into sub-domains already discussed together with Fig. 3, the simulation data have been now stratified by lower tropospheric stability (LST) in Fig. 5. For marine stratiform clouds, LST was found to explain low-level cloud cover to a reasonable degree (see e.g. discussion in Klein and Hartmann, 1993; Wood and Bretherton, 2006). In our simulations, we also identify this ability of LST. We find that average low-level cloud cover increases from 40 % for low LST values around 6 K to almost 75 % for high LST values around 14 K (black curve in Fig. 5a). Additionally, average LWP shows a rapid and more than threefold increase from 60 to 180 $\mathrm{g\,m^{-2}}$ with increasing LST (black curve in Fig. 5b). Thus, due to higher cloud cover and higher LWP, the shortwave cloud-radiative effects become larger leading to decreased shortwave fluxes at the surface (Fig. 5c) and at the TOA (Fig. 5e). Therefore, the lower end of LST marks regions which are either cloud-free or in which small and cumuliform clouds dominate, whereas

the large and thick stratiform cloud decks can be found at higher LST. The anomalies due to aerosol absorption are indicated in Fig. 5 with coloured lines. It can be anticipated that cloud cover changes are largest in convective regions (low LST) and also in the transition zones between convective and stratiform regions (medium LST values in Fig. 5a). In contrast, a reduction found for LWP of $-7\,\mathrm{g\,m^{-2}}$ for high LST is twice as large as the reduction found for low LST (Fig. 5b). Both effects, the reduced low-level cloud cover and the reduced LWP, impact changes of the shortwave fluxes at the surface. The decreased cloud cover lead to more cloud-free areas and thus direct downwelling shortwave fluxes increase, especially for medium LST values (Fig. 5c). This positive flux anomaly is more than compensated by the negative anomaly in the diffuse downwelling shortwave fluxes which also includes the main contributions from aerosol-induced surface dimming (Fig. 5d). The magnitude of the negative diffuse flux anomaly is particularly reduced at high LST where a reduction in LWP causes a thinning of the stratiform cloud field. Thus, the dimming of the surface by absorbing aerosols is compensated by the rapid adjustment of low-level clouds in any regime. However, the actual mechanisms differ for convective regions where a cloud-cover reduction dominates and for stratiform regions where a cloud thinnińg dominates. Furthermore, the shortwave TOA net flux shows a positive anomaly (Fig. 5e) particularly large for medium LST representative for the transition zone between convective and stratiform areas.

For the assessment of the effective radiative forcing, differences in the daily- and domain-average top-of-the-atmosphere (TOA) energy budget are presented in Tab. 1. Aerosol absorption mainly acts on the shortwave component. The net shortwave TOA radiation fluxes increase by 4.5 and 5.1 $\mathrm{W\,m^{-2}}$ in the 625 and 312 m resolution runs, respectively. Thus, the additional absorption leads to the situation where more solar energy is kept in the atmosphere and less is scattered back to space. The difference in the longwave TOA radiation fluxes is of the same, positive, sign, but only marginally contributes to the positive radiative forcing caused by a slightly increased atmospheric opacity. Since the net TOA radiation fluxes are much smaller in magnitude than either the negative longwave and positive shortwave TOA radiation fluxes, and since the perturbations in shortwave and longwave fluxes are of the same sign, the difference in the net TOA radiation of around $5\,\mathrm{W\,m^{-2}}$ substantially changes the rather sensitive net TOA energy budget by $\approx 15\%$.

	625 m	**312 m**
ΔSW_{TOA}	4.46 (1.8%)	5.06 (2.0%)
ΔLW_{TOA}	0.54 (–0.2%)	0.23 (–0.1%)
ΔNET_{TOA}	4.99 (15.1%)	5.29 (17.1%)

TABLE 1 Daily- and domain-average differences of TOA energy budget. For the difference, the purely scattering experiment is subtracted from the experiment with realistic aerosol absorption. Model grid spacing (either 625 or 312 m) is indicated. Absolute differences are in $\mathrm{W\,m^{-2}}$, differences relative to the "scattering" experiment are provided in parenthesis. Fluxes are positive downward, i.e. positive values indicate that the Earth system gains energy.

Absorbing aerosol induces a dimming of downwelling shortwave radiation fluxes at the surface (see Tab. 2). The downwelling shortwave component is reduced by 4 to 4.5 $\mathrm{W\,m^{-2}}$ ($\approx 2\%$) supporting the arguments laid out in Sect. 2.2. Due to the high average total cloud cover of around 80%, the largest contribution to the surface dimming originates from the diffuse downwelling shortwave radiation. The increased thermal opacity of the atmosphere including absorbing aerosol causes an increase in downwelling longwave radiation at the surface which has a magnitude similar to the increase of longwave TOA radiation. The land surface adjusts to the decreased availability in solar energy. Surface temperatures start to decrease as a reaction to this. Consequently, sensible and latent heat fluxes at the

surface also decrease by around 1.5 and 0.6 W m^{-2}, respectively. The reduction in turbulent surface fluxes does not completely compensate the net radiative perturbation. A net energy imbalance of around −1 W m^{-2} remains at the surface which further reduces the surface temperature. Taking the difference between changes at TOA and the surface, the atmosphere absorbs around 8.5 W m^{-2}. Thus, the change of net TOA radiation fluxes is a factor of 0.6 smaller than the change of radiation absorbed in the atmosphere. For anthropogenic aerosol, this factor ranges between -0.3 and -0.1 due to the predominance of scattering sulphate aerosol (Bellouin et al., 2020). When normalised by the applied aerosol perturbation of 0.017 (see Sect. 2.2), the normalised radiation absorbed by the atmosphere is around 500 W m^{-2} similar to Myhre et al. (2013a) who reported values around 525±165 W m^{-2} for global climate model simulations.

	625 m	**312 m**
$\Delta SW_{s,\downarrow}$	−4.46 (−2.2%)	−3.97 (−2.0%)
$\Delta SW_{s,diff,\downarrow}$	−3.58 (−3.6%)	−3.60 (−3.6%)
$\Delta SW_{s,dir,\downarrow}$	−0.88 (−0.9%)	−0.37 (−0.4%)
$\Delta SW_{s,\uparrow}$	0.63 (−2.0%)	0.56 (−1.8%)
$\Delta LW_{s,\downarrow}$	0.49 (0.2%)	0.34 (0.1%)
$\Delta LW_{s,\uparrow}$	0.09 (0.0%)	0.07 (0.0%)
$\Delta SH_{s,\uparrow}$	1.46 (−5.0%)	1.45 (−4.9%)
$\Delta LH_{s,\uparrow}$	0.68 (−1.2%)	0.60 (−1.0%)
ΔNET_s	−1.12 (−3.4%)	−0.96 (−3.2%)

TABLE 2 Differences in daily-average surface energy budget similar to Table 1. Upwelling and downwelling flux differences are indicated by upward and downward directed arrows, respectively. Fluxes are again defined to be positive when downward meaning that positive values indicate that the atmosphere looses energy. $\Delta SW_{s,diff,\downarrow}$ and $\Delta SW_{s,dir,\downarrow}$ are the diffuse and direct components of downwelling shortwave radiation, respectively, and $\Delta LH_{s,\uparrow}$ and $\Delta SH_{s,\uparrow}$ are the latent and sensible turbulent heat fluxes, respectively. ΔNET_s is the sum of the radiative and turbulent energy fluxes, i.e. the heat storage rate of the ground.

As the ICON-LEM is an extension of a numerical weather prediction system to resolutions at hectometre scale, aerosol forcing estimates have not been implemented as a standard online diagnostic. The implementation of this feedback and especially the corresponding re-runs of all numerical experiments are rather cumbersome. Therefore, the aerosol effect is considered here only in an approximated way. A more accurate assessment of the aerosol forcing components with ICON-LEM will be postponed to future studies.

In the following, we make use of the fact that planetary albedo α is highly sensitive to changes in total cloud cover CC_{tot} (Bender et al., 2016). In the cloud cover range that is realised in our simulations, planetary albedo can be approximated by a linear function of total cloud cover (see Fig. 6). For the "scattering" as well as the "absorbing" experiment, a change of 1.2% in albedo is found for a change of 1% in total cloud cover (marked by the two regression lines in Fig. 6). In the temporal average, the planetary albedo of the "scattering" experiment is 35.8%. In the "absorbing" experiment, the planetary albedo is −1.1% lower, i.e. seen from space the effect of the absorbing aerosol is that the Earth appears darker. This darkening occurs for two reasons: first, the absorbing aerosol itself reduces the amount of reflected shortwave radiation at TOA and second, the reduction in cloud cover opens the view onto the Earth's surface

in some regions which have a lower albedo than the more reflective clouds. From the values above, it is also clear that the perturbation of the planetary albedo due to aerosol absorption $\Delta\alpha$ is small which makes us confident that a separation into two distinct parts $\Delta\alpha = \Delta\alpha_{\text{direct}} + \Delta\alpha_{\text{semi}}$ is meaningful. The first term, $\Delta\alpha_{\text{direct}}$, is the albedo change due to direct absorbing aerosol forcing which could have been determined by a second call of the radiation scheme without aerosol absorption. The second term $\Delta\alpha_{\text{semi}}$ is related to the albedo change from semi-direct responses of the atmosphere to absorbing aerosol forcing (rapid adjustments to aerosol-radiation interactions). We have seen that cloud cover is the major control for planetary albedo. Therefore, the semi-direct albedo change is set to be proportional to the cloud cover change, i.e. $\Delta\alpha_{\text{semi}} \approx (\partial\alpha/\partial \text{CC}_{\text{tot}})\,\Delta\text{CC}_{\text{tot}}$. Utilising that the total cloud cover changes from 81.2% in the "scattering" experiment down to 80.8% in the "absorbing" experiment, i.e. $\Delta\text{CC}_{\text{tot}} = -0.4\%$, we find a planetary albedo change due to semi-direct effects in the order of $\Delta\alpha_{\text{semi}} = -0.5\%$. Consequently, the remaining albedo change needs to be attributed to direct absorbing aerosol effects, i.e. $\Delta\alpha_{\text{direct}} = -0.6\%$. As a slightly different derivation, the distance between the two regression lines is an approximation to the albedo change due to absorption. In summary, we find nearly equal direct and semi-direct effects due to aerosol absorption in our simulations.

3.3 | Responses of Liquid Water Path and Precipitation

Aerosol-induced changes in clouds do not only influence the atmospheric energy budget, but also impact the hydrological cycle (Ming et al., 2010). To shed light on this aspect, simulated fields of liquid water path and surface precipitation are analysed in the following.

For our simulations, a negative LWP anomaly develops over time due to the effect of absorbing aerosol. An average LWP of around 95 gm^{-2} is found for the "scattering" experiment when averaged between 8 and 14z. The average LWP is reduced by 4 to 5 gm^{-2} when aerosol absorption is taken into account. In line with the reasoning discussed earlier for low-level cloud cover, reduced relative humidity in the cloud layer and increased stability in the planetary boundary layer have a negative impact on the formation of liquid clouds. The LWP probability density functions (PDFs) for the "scattering" experiment peak around 100 gm^{-2} (see Fig. 7a). The negative anomaly of average LWP comes along with a shift of the LWP PDFs to smaller values which becomes larger as time evolves. We thus see that in terms of a relative distribution, more LWP values smaller and less LWP larger than 80 gm^{-2} are found due to absorbing aerosol. However, this relative shift in LWP PDFs obscures the fact that the smaller LWP values ($< 80\ \text{gm}^{-2}$) still provide the same contribution to the total liquid water mass. The negative LWP anomaly essentially originates from reduced contributions of LWP-values around 200 gm^{-2} (see Fig. 7b).

Next, we analyse which cloud sizes particularly contribute to this reduction in LWP. A value of 200 gm^{-2} is taken as threshold for the LWP-fields which corresponds to the peak in LWP contributions (Fig. 7b). From the resulting binary masks, object size statistics have been derived (see Sect. 2.3). Taking all LWP objects together, the accumulated coverage reduces from 15.1 % in the "scattering" experiment to 14.3 % in the "absorbing" experiment. LWP objects with a diameter around 200 km dominate the overall change and contribute around −0.5 % to the total reduction of −0.8 % (see Fig. 7c). Hence, the large, more stratiform cloud field responds most strongly to the aerosol perturbation. LWP objects smaller than 20 km also contribute to the reduction of areal coverage, but with around -0.3 % in a slightly less pronounced way.

Moreover, the applied method allows to distinguish LWP objects that occur in same locations and thus match between the "scattering" and the "absorbing" experiments, and those for which no local match is identified. The latter are typically rather small (< 20 km) convective LWP objects which appear at displaced locations due to slightly changed convective trigger conditions. The set of matching objects dominates the areal coverage in terms of absolute values. About twenty times more area is covered by all matching objects than by all non-matching objects. Nonetheless, one

quarter of the change in areal coverage between "scattering" and "absorbing" experiments comes from non-matching objects which is a non-negligible contribution. Hence, we find that both, the stratiform and the convective cloud developments, are negatively influenced by the applied aerosol perturbation that jointly induces a heating of the atmospheric boundary layer and a reduction of net radiation at the surface.

The changes in cloud liquid water and the energy budgets have the potential to impact precipitation (see Fig. 8). Slightly different daily rain accumulations are found for different grid spacings (3.2 mm for 625 m and 3.0 mm for 312 m). A similar sensitivity of precipitation to grid spacing in ICON has also been identified in Stevens et al. (2020) and is further discussed, there. On a daily average basis, the relative change in precipitation due to the impact of absorbing aerosol is rather weak, $< 1\%$, and an order of magnitude smaller than the sensitivity to horizontal resolution. The clearest impact on precipitation is identified before individual convective events in the afternoon introduce much more randomness in the temporal evolution of rain. If we only consider the time between 8z and 12z, the domain-averaged rain accumulates only to 0.15 mm (0.09 mm) for 625 m (312 m) grid spacing which is reduced by -5 to $-7\,\%$ due to the effect of absorbing aerosol (see thin solid lines in Fig. 8). Thus, until afternoon, precipitation and LWP reduce by similar relative amounts. Due to the effect of surface dimming, latent heat fluxes and consequently evaporative water fluxes from the surface to the atmosphere are reduced. As time proceeds, the perturbations from precipitation and evaporation start to balance each other and no systematic difference in the net water transfer between the surface and the atmosphere is found. Remarkably, the earlier identified positive perturbation of boundary-layer humidity can not be explained by the change in the surface water budget which would rather suggest a reduction of humidity. Thus, this effect needs to be attributed to changes in the re-distribution of moisture in the atmosphere by changing circulations.

4 | DISCUSSION

The interpretation of aerosol perturbation experiments using regional high-resolution simulations is challenging. The spatial and temporal scales are so different to the scales of global climate models that it is by far not trivial to derive implications for climate-relevant aerosol-radiation interactions from our results. We therefore use this section to discuss our results in the light of other studies, but also clarify weaknesses and caveats.

Substantial reduction of cloud cover over land was also identified by many prior studies on the semi-direct forcing of absorbing aerosol (Koren et al., 2004; Feingold et al., 2005; Huang et al., 2016). Different cloud cover changes have been found which depend on the absorption strength of the aerosols and on the overall average cloud cover, among several other factors. Since the absorption of solar radiation, and thus atmospheric heating, increases proportional to absorption strength (Wild, 2009), it is expected that larger reductions in cloud cover can also be found with larger perturbations in the absorbing aerosol. The cloud-cover sensitivity, which considers the change in cloud cover per absorption AOD, is about $60\,\% \, (\Delta\tau_{\text{abs}})^{-1}$ for our simulations, where $\Delta\tau_{\text{abs}}$ denotes the perturbation of the absorption AOD. Sensitivity values estimated from the literature show a large range for very different reasons, e.g. from $24\,\% \, (\Delta\tau_{\text{abs}})^{-1}$ (Persad et al., 2017) to $80\,\% \, (\Delta\tau_{\text{abs}})^{-1}$ (Feingold et al., 2005) and $85\,\% \, (\Delta\tau_{\text{abs}})^{-1}$ (Koren et al., 2008, for cloud cover of 50% and single scattering albedo of 0.9). Koren et al. (2008) discussed a conceptual model of absorption effects on cloud cover and clarified that the cloud-cover sensitivity varies strongly with the overall average cloud cover and becomes largest for small cloud cover amounts, i.e. for large clear-sky fractions. Furthermore, a potential reduction of evaporative fluxes at the surface might play a role and additionally weakens the formation of boundary layer clouds (Feingold et al., 2005). Also for these surface effects it can be expected that larger perturbations happen at small cloud fractions. Thus, the differently acting mechanisms of surface dimming and atmospheric heating need to

be disentangled in a more systematic way, for instance using the approach of Persad et al. (2017). In the latter study, effects of absorbing aerosol on the East Asian summer monsoon were separated by the help of idealised radiative perturbations that mimic pure dimming, pure heating and pure absorption. Furthermore, the vertical distribution of absorbing aerosol matters for the expected effects on cloud cover. We applied a rather simplified aerosol perturbation with a prescribed vertical profile and a very coarse spatial structure. After the classification framework provided by Koch and Del Genio (2010), the perturbation in our experiments falls into the categories of absorbing aerosols within and below the cloud layers. Variations in the vertical profile of absorbing aerosol can be relatively easily accommodated in future studies of semi-direct effects over Central Europe to assess how rapid cloud adjustments map onto the classification by Koch and Del Genio (2010).

For Central Europe, Meier et al. (2012) conducted realistic aerosol perturbation experiments and found a reduction in cloud cover by 1%, corresponding to a sensitivity of $50\,\%\,(\Delta\tau_{\mathrm{abs}})^{-1}$. In contrast to our study, their simulations were much coarser with a horizontal grid spacing of 28 km and aerosol was set to be completely transparent for their reference calculations, thus including the effects of aerosol scattering in their aerosol forcing estimates. As result, their TOA direct radiative forcing was negative and dominated by aerosol scattering. Surface dimming was a factor of three to four stronger than in our simulations for the same cloud-cover response. This opens room for speculations: Is it possible that the feedbacks due to surface-boundary layer coupling are very sensitive to model resolution and may be underestimated at coarser resolutions? In that case, climate models would underestimate the response of low-level cloud cover to aerosol-induced surface dimming over land. Alternatively, it could be that our analysed cloud scenery is especially sensitive to aerosol perturbations and not representative for other weather regimes and larger areas.

In addition to ARI, aerosols cause changes in the cloud droplet size distributions of low-level clouds and influence microphysical process rates that ultimately affect how much sunlight clouds reflect and when and how much rain falls. This microphysical pathway was intentionally excluded in our study. The effective radiative forcing of ACI is believed to be negative and between -1.7 and $-0.3\,\mathrm{W\,m^{-2}}$ on a global scale (Bellouin et al., 2020), and thus ACI has the potential to compensate positive forcings by strongly absorbing aerosols. A negative forcing from ACI was also reported by Costa-Surós et al. (2020) in a regional modelling study with same ICON-LEM model and also for the same simulation period. They applied aerosol perturbations representing the difference between European peak-aerosol conditions in 1985 and current aerosol levels (represented by the year 2013) and estimated CCN concentrations that impact ICON cloud microphysics via aerosol-cloud interactions. Costa-Surós et al. (2020) could show that an applied increase in CCN concentrations by a factor of 2 to 5 in the planetary boundary layer leads to accordingly higher cloud-droplet number concentrations and thus higher cloud albedo. An effective solar radiative forcing due to cloud-aerosol interaction of $-2.6\,\mathrm{W\,m^{-2}}$ was derived. Hence, that effect has a magnitude similar to the individually estimated effects of direct and semi-direct forcing due to aerosol absorption which are found here to be rather similar and both together sum up to $4.5\,\mathrm{W\,m^{-2}}$ (see Table 1). Moreover, the authors found a reduction of rain water mass that was to a large extent compensated by increase of non-precipitating LWP (a LWP difference of around $7\,\mathrm{g\,m^{-2}}$ on average). In comparison to our results, the underlying mechanism for the rain reduction is however very different: While CCN perturbations cause changes in efficiency for the conversion between cloud condensate and precipitation, i.e. how fast the water substance is removed from the atmosphere, the perturbations in aerosol absorption impact the evaporative surface fluxes and thus determine how much water is made available from the surface. Therefore and in contrast to Costa-Surós et al. (2020), our simulation experiments show consistent decreases in LWP and accumulated rain.

In the following, some limitations of our study are discussed. We considered only one specific day during mid-latitude spring. Although the case offered a good mixture of convective and stratiform clouds, it is not clear to what

extent similar responses can be found for different weather situations. However, it has been discussed by Nam et al. (2018) that atmospheric processes influencing shortwave rapid cloud adjustments over Central Europe are mainly caused by local cloud dynamics and are, for shorter time periods, rather independent of the synoptic-scale circulations. Nam et al. (2018) further argued that mechanisms that lead to rapid cloud adjustments over Central Europe are representative for the continental Northern Hemisphere and that such high-resolution simulations like ours can be helpful for assessing and constraining global rapid cloud adjustments. An other shortcoming is that the applied aerosol perturbation leads to a transient atmospheric response that has not reached equilibrium within the short integration time and over the limited domain size. We find that less energy is radiated away at the TOA, but also less energy reaches the Earth surface. Therefore, the atmosphere continuously gains energy which would lead to a secular increase of the atmospheric energy content over time. Such a behaviour is obviously unrealistic and mechanisms that buffer the atmospheric response need to be considered for longer integrations. Therefore, energy and moisture need to be freely exchanged across the boundaries of the limited-area domain. Feedbacks onto synoptic-scale circulation systems will become more relevant for time scales longer than a few days (Nam et al., 2018).

All scientific conclusions would benefit from a systematic approach that is able to distinguish between the rather random disturbances introduced by different weather pathways and the causal response of the atmosphere to aerosol perturbations. We examined simulations at two different horizontal resolutions to assess the robustness of the identified anomalies. A statistical ensemble approach in which initial or boundary conditions experience small random perturbations might be better suited to increase confidence in the magnitude of the aerosol effects, especially with regard to effects on mixed-phase clouds, cirrus and precipitation formation. Nonetheless, our study and high-resolution simulations in general provide useful insights into the response of low-level clouds over heterogeneous land surfaces. Two aspects that are in particular advantageous in such a setup are: (i) cloud-scale circulation anomalies can be at least partly resolved, and (ii) due to the coupling of the atmosphere to a sophisticated surface model, the atmospheric response to dimming is represented with considerable detail.

5 | SUMMARY

Depending on composition, atmospheric aerosol particles can absorb solar radiation. These absorbing aerosol alter the thermal structure of the atmosphere by their local heating (Ramanathan et al., 2001). Moreover, absorbing aerosol also hinder solar radiation from reaching the surface which leads the changes in sensible and latent heat fluxes at the surface. All these aerosol-induced impacts change atmospheric conditions in a rather complex manner and can induce rapid cloud adjustments that can either compensate the direct aerosol forcing or even amplify it (Bond et al., 2013). Absorbing aerosol largely originates from anthropogenic activities such as black carbon from fossil fuel burning and combustion (Bond et al., 2013). Thus, absorbing aerosol contribute to the human impact on climate as a so-called "short-lived climate forcer" and it is considered that reducing black carbon emissions will support reducing the anthropogenic climate effect. Lowering the uncertainties in our understanding of so-called aerosol-radiation interactions is therefore of tremendous importance (Boucher et al., 2013; Bellouin et al., 2020).

In our study, we approached the topic of aerosol-radiation interactions from a large-domain, high-resolution modelling perspective. This especially helps to represent the cloud-induced circulation anomalies that develop in response to aerosol effects. Furthermore, a realistic coupling of the atmosphere to the underlying surface is in particular important for low-level cloud feedbacks over land (Feingold et al., 2005) where latent and sensible heat fluxes rapidly adjust to changes in incoming solar radiation. For these reasons, we investigated the sensitivity of simulations of the ICON model over Central Europe. We performed simulations with a horizontal grid spacing of 312 m and 625 m which

at least partially allows to resolve cloud-induced circulations. For one case day in mid-latitude spring, simulation experiments with different aerosol radiative properties have been performed without the modification of aerosol-cloud interactions. A high-resolution simulation with aerosol loads and absorption properties comparable to current levels has been contrasted to a simulation with aerosol absorption set to zero. In this way, changes in the thermal structure of the atmosphere as well as changes in cloud cover and atmospheric radiation fluxes are attributed to the effect of aerosol absorption. The applied aerosol perturbation is constructed to be strongest in the planetary boundary layer, thus having also the strongest impact on low-level clouds.

Based on the analysis of our perturbation experiments, following main conclusions can be formulated for the considered region in Central Europe and for the studied case day:

(i) Absorbing aerosol particles induce a reduction of downwelling shortwave radiation fluxes ($\Delta SW_{s,\downarrow} \approx -4\,Wm^{-2}$ on daily average, especially from diffuse shortwave radiation) which in turn leads to reduced surface latent and sensible heat fluxes.

(ii) A warm and dry anomaly develops in the low-level cloud layer around 850 hPa due to the combined impact of atmospheric heating and surface dimming from absorbing aerosol. As result, cloud cover at this altitude reduces by around −1%.

(iii) The decreased transfer of moisture and energy from the surface to the atmosphere leads to less convective cloud development and to a thinning of stratiform cloud decks. Both feedbacks can be interpreted as rapid adjustments of low-level clouds in either the convective or the stratiform cloud regime that compensate or buffer aerosol-induced surface dimming.

(iv) Net TOA radiation fluxes increase by around $5\,Wm^{-2}$ indicating a positive radiative forcing in which the atmosphere gains energy. Radiative forcing from direct and semi-direct aerosol effects are both positive and have similar magnitudes.

(v) Domain-average values of LWP and precipitation reduce by similar amounts (−5 to −7%) until afternoon due to the decreased availability of moisture from the surface. Changes in LWP are dominated by a shrinking of large, stratiform cloud decks. Moreover, also the number of small, convective clouds is diminished by aerosol absorption.

In our discussion section 4, we suggested several directions to expand the current study. Our understanding of regional effects of aerosol-radiation interactions will benefit from pursuing further high-resolution sensitivity experiments for different weather situation and for different types of aerosol perturbations. In addition, a future study that separates the effects of surface dimming and atmospheric heating in this high-resolution modelling setup would be very insightful. Even if all these attempts remain rather idealised, an approach such as described in our study helps to build a conceptual view on cloud feedbacks to aerosol perturbations on a regional level.

acknowledgements

FS thanks Olaf Hellmuth for his comments on an earlier version of this study. Catrin Meyer and the RZ Jülich are acknowledged for conducting the ICON simulation experiments and providing computing resources, respectively. DKRZ is acknowledged for providing storage and post-processing resources within the projects bm0834 and bb1174.

Open science: Analysis data have been collected at the long-term archive (LTA) of DKRZ and can be assessed under `https://cera-www.dkrz.de/WDCC/ui/cerasearch/entry?acronym=DKRZ_LTA_1174_ds00001`. The analysis source code has been made freely available to improve reproducibility of our results. The final plots for our paper were done with Jupyter Notebooks which are published at `https://zenodo.org/record/5078285`.

references

Ackerman, A. S., Toon, O. B., Stevens, D. E., Heymsfield, A. J., Ramanathan, V. and Welton, E. J. (2000) Reduction of tropical cloudiness by soot. *Science*, **288**, 1042–1047.

Baldauf, M., Seifert, A., Förstner, J., Majewski, D., Raschendorfer, M. and Reinhardt, T. (2011) Operational Convective-Scale Numerical Weather Prediction with the COSMO Model: Description and Sensitivities. *Mon. Wea. Rev.*, **139**, 3887–3905.

Bellouin, N., Quaas, J., Gryspeerdt, E., Kinne, S., Stier, P., Watson-Parris, D., Boucher, O., Carslaw, K., Christensen, M., Daniau, A.-L., Dufresne, J.-L., Feingold, G., Fiedler, S., Forster, P., Gettelman, A., Haywood, J. M., Lohmann, U., Malavelle, F., Mauritsen, T., McCoy, D., Myhre, G., Mülmenstädt, J., Neubauer, D., Possner, A., Rugenstein, M., Sato, Y., Schulz, M., Schwartz, S. E., Sourdeval, O., Storelvmo, T., Toll, V., Winker, D. and Stevens, B. (2020) Bounding global aerosol radiative forcing of climate change. *Rev. Geophys.*, **58**, e2019RG000660.

Bender, F. A.-M., Engström, A. and Karlsson, J. (2016) Factors Controlling Cloud Albedo in Marine Subtropical Stratocumulus Regions in Climate Models and Satellite Observations. *Journal of Climate*, **29**, 3559–3587.

Bond, T. C., Doherty, S. J., Fahey, D. W., Forster, P. M., Berntsen, T., DeAngelo, B. J., Flanner, M. G., Ghan, S., Kärcher, B., Koch, D., Kinne, S., Kondo, Y., Quinn, P. K., Sarofim, M. C., Schultz, M. G., Schulz, M., Venkataraman, C., Zhang, H., Zhang, S., Bellouin, N., Guttikunda, S. K., Hopke, P. K., Jacobson, M. Z., Kaiser, J. W., Klimont, Z., Lohmann, U., Schwarz, J. P., Shindell, D., Storelvmo, T., Warren, S. G. and Zender, C. S. (2013) Bounding the role of black carbon in the climate system: A scientific assessment. *J. Geophys. Res. Atmos.*, **118**, 5380–5552.

Boucher, O., Randall, D., Artaxo, P., Bretherton, C., Feingold, G., Forster, P., Kerminen, V.-M., Kondo, Y., Liao, H., Lohmann, U. et al. (2013) Clouds and aerosols. In *Climate change 2013: The physical science basis. Contribution of working group I to the fifth assessment report of the intergovernmental panel on climate change*, 571–657. Cambridge University Press.

Chand, D., Wood, R., Anderson, T., Satheesh, S. and Charlson, R. (2009) Satellite-derived direct radiative effect of aerosols dependent on cloud cover. *Nat. Geosci.*, **2**, 181–184.

Costa-Surós, M., Sourdeval, O., Acquistapace, C., Baars, H., Carbajal Henken, C., Genz, C., Hesemann, J., Jimenez, C., König, M., Kretzschmar, J., Madenach, N., Meyer, C. I., Schrödner, R., Seifert, P., Senf, F., Brueck, M., Cioni, G., Engels, J. F., Fieg, K., Gorges, K., Heinze, R., Siligam, P. K., Burkhardt, U., Crewell, S., Hoose, C., Seifert, A., Tegen, I. and Quaas, J. (2020) Detection and attribution of aerosol–cloud interactions in large-domain large-eddy simulations with the icosahedral nonhydrostatic model. *Atmos. Chem. Phys.*, **20**, 5657–5678. URL: https://www.atmos-chem-phys.net/20/5657/2020/.

Curci, G., Alyuz, U., Barò, R., Bianconi, R., Bieser, J., Christensen, J. H., Colette, A., Farrow, A., Francis, X., Jiménez-Guerrero, P., Im, U., Liu, P., Manders, A., Palacios-Peña, L., Prank, M., Pozzoli, L., Sokhi, R., Solazzo, E., Tuccella, P., Unal, A., Vivanco, M. G., Hogrefe, C. and Galmarini, S. (2019) Modelling black carbon absorption of solar radiation: combining external and internal mixing assumptions. *Atmos. Chem. Phys.*, **19**, 181–204. URL: https://acp.copernicus.org/articles/19/181/2019/.

Davis, C. A., Brown, B. G., Bullock, R. and Halley-Gotway, J. (2009) The method for object-based diagnostic evaluation (mode) applied to numerical forecasts from the 2005 Nssl/spc spring program. *Wea. Forecasting*, **24**, 1252–1267. URL: http://dx.doi.org/10.1175/2009WAF2222241.1.

Dipankar, A., Stevens, B., Heinze, R., Moseley, C., Zängl, G., Giorgetta, M. and Brdar, S. (2015) Large eddy simulation using the general circulation model icon. *J. Adv. Model. Earth Syst.*, **7**, 963–986. URL: http://dx.doi.org/10.1002/2015MS000431.

Ebert, E., Wilson, L., Weigel, A., Mittermaier, M., Nurmi, P., Gill, P., Göber, M., Joslyn, S., Brown, B., Fowler, T. and et al. (2013) Progress and challenges in forecast verification. *Meteorological Applications*, **20**, 130–139. URL: http://dx.doi.org/10.1002/met.1392.

Feingold, G., Jiang, H. and Harrington, J. Y. (2005) On smoke suppression of clouds in amazonia. *Geophys. Res. Lett.*, **32**, L02804. URL: https://agupubs.onlinelibrary.wiley.com/doi/abs/10.1029/2004GL021369.

Flato, G., Marotzke, J., Abiodun, B., Braconnot, P., Chou, S. C., Collins, W., Cox, P., Driouech, F., Emori, S., Eyring, V. et al. (2014) Evaluation of climate models. In *Climate change 2013: the physical science basis. Contribution of Working Group I to the Fifth Assessment Report of the Intergovernmental Panel on Climate Change*, 741–866. Cambridge University Press.

Genz, C., Schrödner, R., Heinold, B., Henning, S., Baars, H., Spindler, G. and Tegen, I. (2020) Estimation of cloud condensation nuclei number concentrations and comparison to in situ and lidar observations during the hope experiments. *Atmos. Chem. Phys.*, **20**, 8787–8806. URL: https://acp.copernicus.org/articles/20/8787/2020/.

Gilleland, E., Ahijevych, D., Brown, B. G., Casati, B. and Ebert, E. E. (2009) Intercomparison of spatial forecast verification methods. *Wea. Forecasting*, **24**, 1416–1430. URL: http://dx.doi.org/10.1175/2009WAF2222269.1.

Gordon, H., Field, P. R., Abel, S. J., Dalvi, M., Grosvenor, D. P., Hill, A. A., Johnson, B. T., Miltenberger, A. K., Yoshioka, M. and Carslaw, K. S. (2018) Large simulated radiative effects of smoke in the south-east atlantic. *Atmos. Chem. Phys.*, **18**, 15261–15289.

Grassl, H. (1975) Albedo reduction and radiative heating of clouds by absorbing aerosol particles. *Contrib. Atmos. Phys.*, **48**, 199–210.

Hansen, J., Sato, M. and Ruedy, R. (1997) Radiative forcing and climate response. *J. Geophys. Res.*, **102**, 6831–6864.

Heikenfeld, M., Marinescu, P. J., Christensen, M., Watson-Parris, D., Senf, F., van den Heever, S. C. and Stier, P. (2019) tobac 1.2: towards a flexible framework for tracking and analysis of clouds in diverse datasets. *Geosci. Model Dev.*, **12**, 4551–4570. URL: https://www.geosci-model-dev.net/12/4551/2019/.

Heinze, R., Dipankar, A., Henken, C. C., Moseley, C., Sourdeval, O., Trömel, S., Xie, X., Adamidis, P., Ament, F., Baars, H., Barthlott, C., Behrendt, A., Blahak, U., Bley, S., Brdar, S., Brueck, M., Crewell, S., Deneke, H., Girolamo, P. D., Evaristo, R., Fischer, J., Frank, C., Friederichs, P., Göcke, T., Gorges, K., Hande, L., Hanke, M., Hansen, A., Hege, H.-C., Hoose, C., Jahns, T., Kalthoff, N., Klocke, D., Kneifel, S., Knippertz, P., Kuhn, A., van Laar, T., Macke, A., Maurer, V., Mayer, B., Meyer, C. I., Muppa, S. K., Neggers, R. A. J., Orlandi, E., Pantillon, F., Pospichal, B., Röber, N., Scheck, L., Seifert, A., Seifert, P., Senf, F., Siligam, P., Simmer, C., Steinke, S., Stevens, B., Wapler, K., Weniger, M., Wulfmeyer, V., Zängl, G., Zhang, D. and Quaas, J. (2017) Large-eddy simulations over germany using ICON: a comprehensive evaluation. *Quart. J. Roy. Meteor. Soc.*, **143**, 69–100.

Heise, E., Ritter, B. and Schrodin, R. (2006) Operational implementation of the multilayer soil model. *Tech. Rep. 9*, Deutscher Wetterdienst, Offenbach, Germany. URL: http://www.cosmo-model.org. (accessed 29 October 2020).

Huang, X., Ding, A., Liu, L., Liu, Q., Ding, K., Niu, X., Nie, W., Xu, Z., Chi, X., Wang, M., Sun, J., Guo, W. and Fu, C. (2016) Effects of aerosol–radiation interaction on precipitation during biomass-burning season in east china. *Atmos. Chem. Phys.*, **16**, 10063–10082. URL: https://acp.copernicus.org/articles/16/10063/2016/.

Klein, S. A. and Hartmann, D. L. (1993) The seasonal cycle of low stratiform clouds. *J. Climate*, **6**, 1587 – 1606. URL: https://journals.ametsoc.org/view/journals/clim/6/8/1520-0442_1993_006_1587_tscols_2_0_co_2.xml.

Koch, D. and Del Genio, A. D. (2010) Black carbon semi-direct effects on cloud cover: review and synthesis. *Atmos. Chem. Phys.*, **10**, 7685–7696. URL: https://www.atmos-chem-phys.net/10/7685/2010/.

Koren, I., Kaufman, Y. J., Remer, L. A. and Martins, J. V. (2004) Measurement of the Effect of Amazon Smoke on Inhibition of Cloud Formation. *Science*, **303**, 1342–1345.

Koren, I., Martins, J. V., Remer, L. A. and Afargan, H. (2008) Smoke invigoration versus inhibition of clouds over the amazon. *Science*, **321**, 946–949.

Liepert, B. G. (2002) Observed reductions of surface solar radiation at sites in the united states and worldwide from 1961 to 1990. *Geophys. Res. Lett.*, **29**, 1421.

Lin, Y., Fan, J., Jeong, J.-H., Zhang, Y., Homeyer, C. R. and Wang, J. (2021) Urbanization-induced land and aerosol impacts on storm propagation and hail characteristics. *J. Atmos. Sci.*, **78**, 925 – 947. URL: https://journals.ametsoc.org/view/journals/atsc/78/3/JAS-D-20-0106.1.xml.

Liu, L., Cheng, Y., Wang, S., Wei, C., Pöhlker, M. L., Pöhlker, C., Artaxo, P., Shrivastava, M., Andreae, M. O., Pöschl, U. and Su, H. (2020) Impact of biomass burning aerosols on radiation, clouds, and precipitation over the amazon: relative importance of aerosol–cloud and aerosol–radiation interactions. *Atmos. Chem. Phys.*, **20**, 13283–13301. URL: https://acp.copernicus.org/articles/20/13283/2020/.

Lohmann, U. and Feichter, J. (2001) Can the direct and semi-direct aerosol effect compete with the indirect effect on a global scale? *Geophys. Res. Lett.*, **28**, 159–161.

Macke, A., Seifert, P., Baars, H., Barthlott, C., Beekmans, C., Behrendt, A., Bohn, B., Brueck, M., Bühl, J., Crewell, S., Damian, T., Deneke, H., Düsing, S., Foth, A., Di Girolamo, P., Hammann, E., Heinze, R., Hirsikko, A., Kalisch, J., Kalthoff, N., Kinne, S., Kohler, M., Löhnert, U., Madhavan, B. L., Maurer, V., Muppa, S. K., Schween, J., Serikov, I., Siebert, H., Simmer, C., Späth, F., Steinke, S., Träumner, K., Trömel, S., Wehner, B., Wieser, A., Wulfmeyer, V. and Xie, X. (2017) The hd(cp)^2 observational prototype experiment (hope) – an overview. *Atmos. Chem. Phys.*, **17**, 4887–4914. URL: https://www.atmos-chem-phys.net/17/4887/2017/.

Meier, J., Tegen, I., Heinold, B. and Wolke, R. (2012) Direct and semi-direct radiative effects of absorbing aerosols in europe: Results from a regional model. *Geophys. Res. Lett.*, **39**. URL: https://agupubs.onlinelibrary.wiley.com/doi/abs/10.1029/2012GL050994.

Ming, Y., Ramaswamy, V. and Persad, G. (2010) Two opposing effects of absorbing aerosols on global-mean precipitation. *Geophys. Res. Lett.*, **37**, L13701.

Mlawer, E. J., Taubman, S. J., Brown, P. D., Iacono, M. J. and Clough, S. A. (1997) Radiative transfer for inhomogeneous atmospheres: RRTM, a validated correlated-k model for the longwave. *J. Geophys. Res. Atmos.*, **102**, 16663–16682.

Myhre, G., Samset, B. H., Schulz, M., Balkanski, Y., Bauer, S., Berntsen, T. K., Bian, H., Bellouin, N., Chin, M., Diehl, T. et al. (2013a) Radiative forcing of the direct aerosol effect from aerocom phase ii simulations. *Atmos. Chem. Phys.*, **13**, 1853–1877.

Myhre, G., Shindell, D., Bréon, F.-M., Collins, W., Fuglestvedt, J., Huang, J., Koch, D., Lamarque, J.-F., Lee, D., Mendoza, B., Nakajima, T., Robock, A., Stephens, G., Takemura, T. and Zhang, H. (2013b) Anthropogenic and natural radiative forcing. In *Climate Change 2013: The Physical Science Basis. Contribution of Working Group I to the Fifth Assessment Report of the Intergovernmental Panel on Climate Change* (eds. T. Stocker, D. Qin, G.-K. Plattner, M. Tignor, S. Allen, J. Boschung, A. Nauels, Y. Xia, V. Bex and P. Midgley). Cambridge, United Kingdom and New York, NY, USA: Cambridge University Press.

Nam, C., Kühne, P., Salzmann, M. and Quaas, J. (2018) A prospectus for constraining rapid cloud adjustments in general circulation models. *J. Adv. Model. Earth Syst.*, **10**, 2080–2094. URL: https://agupubs.onlinelibrary.wiley.com/doi/abs/10.1029/2017MS001153.

Persad, G. G., Paynter, D. J., Ming, Y. and Ramaswamy, V. (2017) Competing atmospheric and surface-driven impacts of absorbing aerosols on the east asian summertime climate. *J. Climate*, **30**, 8929–8949. URL: https://doi.org/10.1175/JCLI-D-16-0860.1.

Petty, G. W. (2006) *A first course in atmospheric radiation*. Sundog Pub.

Ramanathan, V. and Carmichael, G. (2008) Global and regional climate changes due to black carbon. *Nat. Geosci.*, **1**, 221–227.

Ramanathan, V., Crutzen, P. J., Kiehl, J. T. and Rosenfeld, D. (2001) Aerosols, Climate, and the Hydrological Cycle. *Science*, **294**, 2119–2124.

Rempel, M., Senf, F. and Deneke, H. (2017) Object-based metrics for forecast verification of convective development with geostationary satellite data. *Mon. Wea. Rev.*, **145**, 3161–3178.

Seifert, A. and Beheng, K. D. (2005) A two-moment cloud microphysics parameterization for mixed-phase clouds. part 1: Model description. *Meteor. Atmos. Phys.*, **92**, 45– 66. URL: http://dx.doi.org/10.1007/s00703-005-0112-4.

Senf, F., Klocke, D. and Brueck, M. (2018) Size-resolved evaluation of simulated deep tropical convection. *Mon. Wea. Rev.*, **146**, 2161–2182.

Sherwood, S. C., Bony, S., Boucher, O., Bretherton, C., Forster, P. M., Gregory, J. M. and Stevens, B. (2015) Adjustments in the forcing-feedback framework for understanding climate change. *Bull. Amer. Meteorol. Soc.*, **96**, 217–228.

Stevens, B., Acquistapace, C., Hansen, A., and Coauthors incl. Senf, F. (2020) Large-eddy and storm resolving models for climate prediction the added value for clouds and precipitation. *J. Meteor. Soc. Japan*.

Tegen, I., Hollrig, P., Chin, M., Fung, I., Jacob, D. and Penner, J. (1997) Contribution of different aerosol species to the global aerosol extinction optical thickness: Estimates from model results. *J. Geophys. Res. Atmos.*, **102**, 23895–23915.

Weniger, M. and Friederichs, P. (2016) Using the sal technique for spatial verification of cloud processes: A sensitivity analysis. *J. Appl. Meteor. Climatol.*, **55**, 2091–2108. URL: http://dx.doi.org/10.1175/JAMC-D-15-0311.1.

Wilcox, E. M. (2012) Direct and semi-direct radiative forcing of smoke aerosols over clouds. *Atmos. Chem. Phys.*, **12**, 139–149.

Wild, M. (2009) Global dimming and brightening: A review. *J. Geophys. Res. Atmos.*, **114**. URL: https://agupubs.onlinelibrary.wiley.com/doi/abs/10.1029/2008JD011470.

Wood, R. and Bretherton, C. S. (2006) On the relationship between stratiform low cloud cover and lower-tropospheric stability. *J. Climate*, **19**, 6425 – 6432. URL: https://journals.ametsoc.org/view/journals/clim/19/24/jcli3988.1.xml.

Wu, L., Su, H. and Jiang, J. H. (2011) Regional simulations of deep convection and biomass burning over south america: 2. biomass burning aerosol effects on clouds and precipitation. *J. Geophys. Res. Atmos.*, **116**. URL: https://agupubs.onlinelibrary.wiley.com/doi/abs/10.1029/2011JD016106.

Yamaguchi, T., Feingold, G., Kazil, J. and McComiskey, A. (2015) Stratocumulus to cumulus transition in the presence of elevated smoke layers. *Geophys. Res. Lett.*, **42**, 10,478–10,485. URL: https://agupubs.onlinelibrary.wiley.com/doi/abs/10.1002/2015GL066544.

Zängl, G., Reinert, D., Rípodas, P. and Baldauf, M. (2014) The ICon (ICosahedral non-hydrostatic) modelling framework of dwd and MPI-m: Description of the non-hydrostatic dynamical core. *Q.J.R. Meteorol. Soc*, **141**, 563–579. URL: http://dx.doi.org/10.1002/qj.2378.

List of Figures

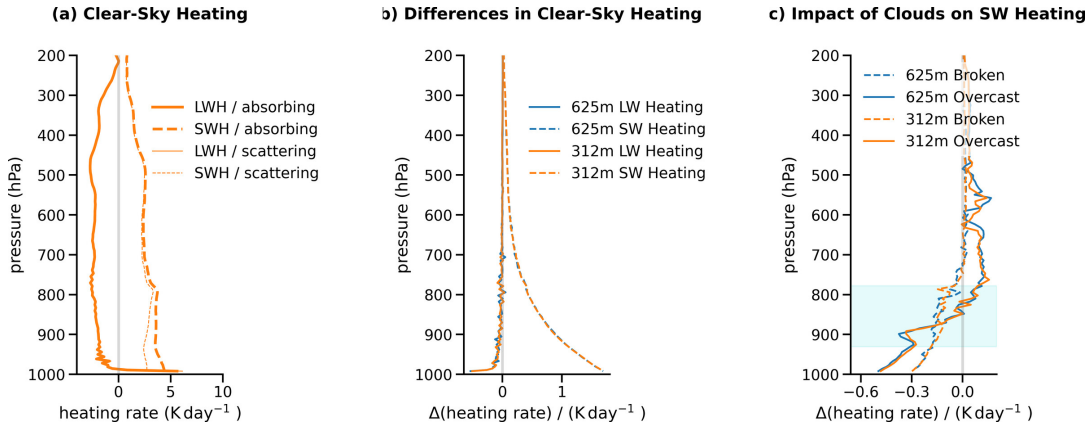

FIGURE 1 Domain-average radiative heating profiles at 11z (local noon). (a) Longwave heating (LWH, solid lines) and shortwave heating (SWH, dashed line) are compared for the two sensitivity experiments "absorbing" (incl. aerosol absorption, thick lines) and "scattering" (excl. aerosol absorption, thin lines) with 312 m grid spacing. Heating rates are derived in clear-sky conditions, i.e. only in regions where total cloud cover is equal zero. (b) The heating rate differences between "absorbing" and "scattering" experiments are shown for 312 m grid spacing (orange) and 625 m grid spacing (blue). (c) Here, the SWH rate differences in clear-sky conditions are subtracted from SWH rate differences in certain cloudy conditions. Overcast (solid lines) refers to regions where total cloud cover averaged in 10 km sub-regions is larger than 95% and broken (clouds, dashed lines) refers to regions with intermediate total cloud cover values between 25 and 75% (again averaged in 10 km sub-regions). The light blue range indicates where a substantial amount of liquid cloud condensate is present.

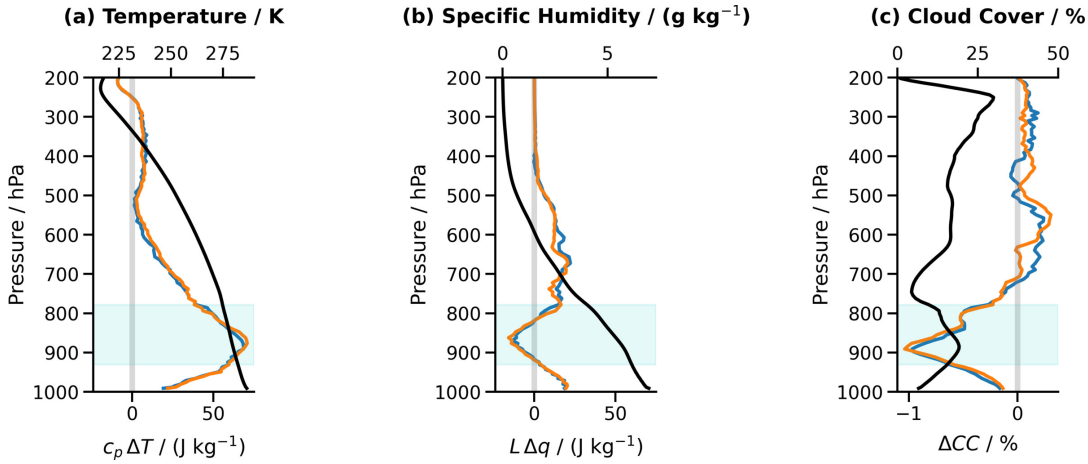

788

789 **FIGURE 2** Domain-average profiles of (a) temperature, (b) specific humidity and (c) cloud cover. The values are
790 averaged for a time period of 8 to 14z. Black lines refer to the absolute values of the respective quantities of the
791 "scattering" experiment as reference case for which the simulations with the two different grid spacings have been
792 averaged. The coloured lines present the absorption-induced differences between the ICON experiments (blue:
793 625 m, orange: 312 m). Enthalpy scaling has been applied to the temperature and humidity differences to make
794 them comparable. The top x-axes provide labels for the absolute quantities, the bottom x-axes provide labels for
796 the differences. The light blue range indicates liquid cloud condensate.

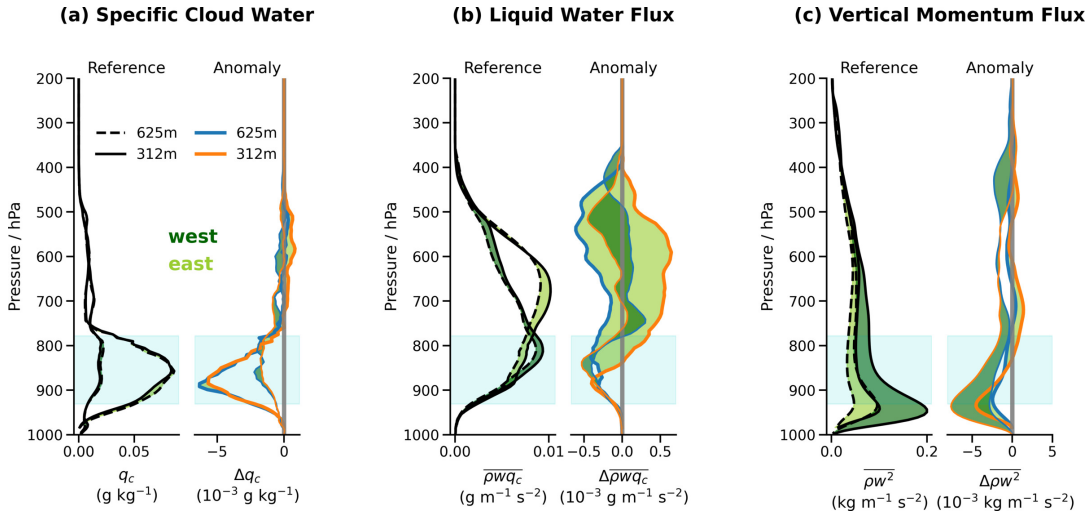

FIGURE 3 Profiles of (a) specific cloud water, (b) liquid water flux and (c) upward flux of vertical momentum. The profiles result from sub-domain averages with "west" indicating all values west of 10°E and "east" for the remaining part. In addition, temporal averaging between 8 and 14z is applied. The black lines refer to the absolute values from reference ("scattering" experiment) for 312 (solid) and 625 m (dashed) grid spacing. The coloured lines present the absorption-induced anomalies (blue: 625 m, orange: 312 m). The space between profiles from identical sub-domains, but differing grid spacing is filled with green shading (dark green: west, light green: east) to visualise the spread due to resolution sensitivity.

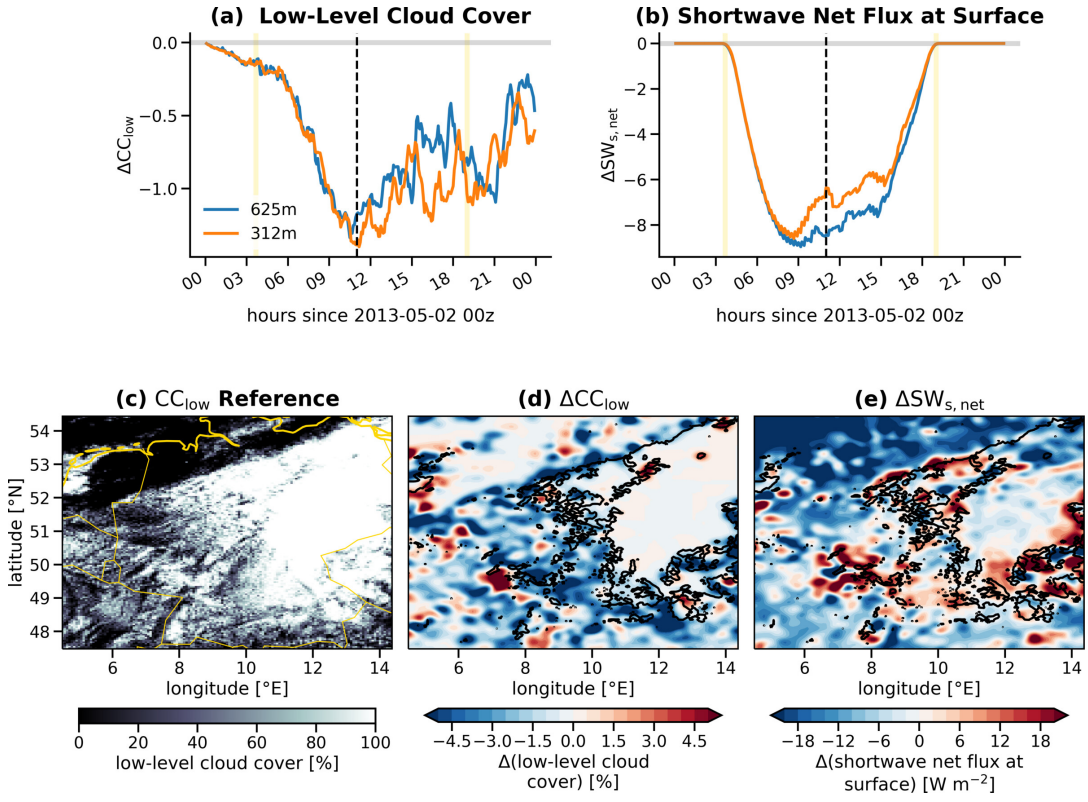

FIGURE 4 Overview of the evolution of low-level cloud cover and resulting changes in shortwave radiation fluxes at the surface. The full time series of (a) low-level cloud cover anomaly and (b) the net shortwave radiation flux anomalies at the surface (sum of up- and downwelling components) are presented for 312 m (orange) and 625 m (blue) grid spacing. Sunrise and sunset are marked by light yellow vertical lines. The bottom row provides an overview of the cloud scenery and resulting anomalies for 312 m and 11z. (c) The low-level cloud cover (CC_{low}) reference is taken from the "scattering" experiment. Coastlines and country borders are outlined in yellow. The anomalies of (d) low-level cloud cover anomaly ΔCC_{low} and (e) net shortwave radiation at the surface have been smoothed with a Gaussian filter of width 2 to improve visibility. The 95%-contour of the CC_{low} reference is shown in (d) and (e) as black line.

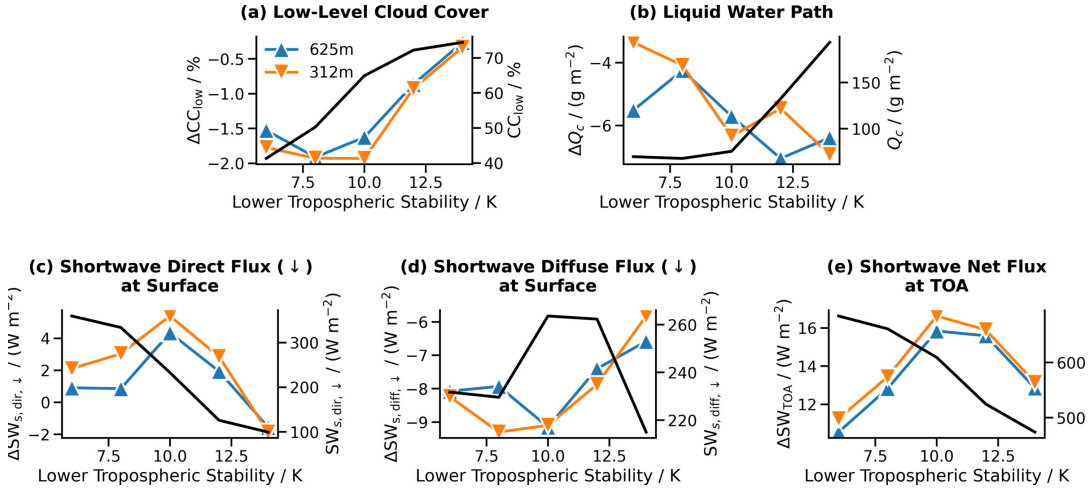

FIGURE 5 Dependency of (a) low-level cloud cover, (b) liquid water path, (c) direct downwelling shortwave radiation flux at surface, (d) diffuse downwelling shortwave radiation flux at surface and (e) shortwave TOA net flux on lower tropospheric stability (LST). LST is defined as difference between virtual potential temperatures at model levels $l = 150$ (lower most level) and $l = 110$ (at around 720 hPa). Data have been binned in 2K-intervals starting at LTS = 5 K and the chosen range includes 92 % of all data. Only domain averages are plotted at the interval mid-point. Black lines refer to the absolute values of the respective quantities of the "scattering" experiment as reference case for which the simulations with the two different grid spacings have been averaged (y-axis is placed on the right side). The coloured lines present the absorption-induced differences between the ICON experiments (blue: 625 m, orange: 312 m) with the y-axis placed on the left side.

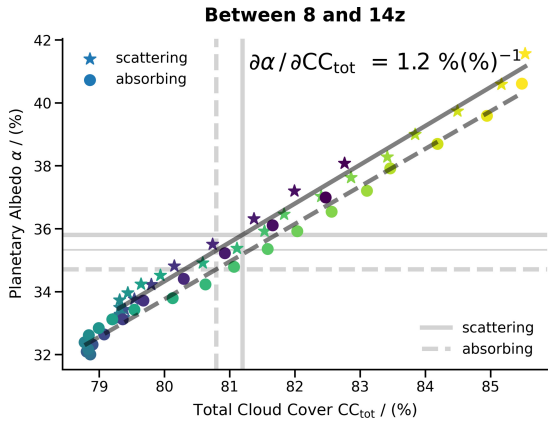

FIGURE 6 Assessing direct vs. semi-direct aerosol effects based on planetary albedo α and total cloud cover CC_{tot}. Coloured symbols represent instantaneous pairs of total cloud cover and planetary albedo (stars: "scattering", circles: "absorbing") between 8 and 14z with a time interval of 15 min. The colours change from 8z (purple) to 11z (blue) and 14z (yellow). The tilted dark grey lines indicate linear regression results and the thick light grey lines show the mean values for planetary albedo (horizontal lines) and total cloud cover (vertical lines) for "scattering" (solid) and "absorbing" (dashed) experiments. The difference between the thick and the thin light grey line (horizontal, solid) indicates how much the planetary albedo is lowered by reducing the cloud amount from the "scattering" to the "absorbing" experiment. It is found by following the solid regression line from the crossing of two thick light grey lines to the vertical dashed light grey line. Only the 625 m simulation is shown here.

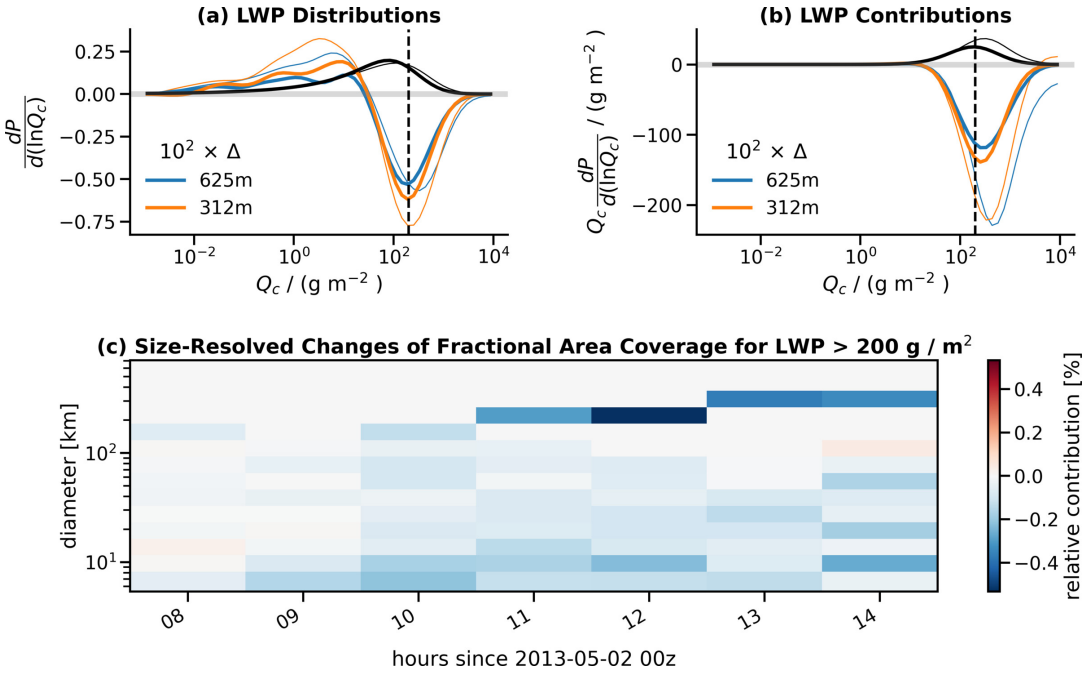

FIGURE 7 Analysis of the LWP fields. Panels (a) and (b) provide LWP probability density functions (LWP is denoted as Q_c in the figure labels and formulas) and the contribution of a $\ln(Q_c)$-interval to the total, domain-average, respectively. The function P defines the probability that Q_c falls into the interval $\ln Q_c \pm d \ln Q_c/2$. Thick lines represent temporal averages between 8 and 11z, thin lines represent averages between 11 and 14z. The black lines are obtained by averaging the two ICON setups ("absorbing", "scattering") and the two different horizontal resolutions. The coloured lines show the difference between the "absorbing" and the "scattering" experiments separately for different resolutions and scaled by a factor of 100 to improve depiction. The vertical dashed line marks the threshold of Q_c = 200 gm^{-2} which was taken to derived size statistics in panel (c). Therein, the difference ("absorbing" vs. "scattering") in fractional area covered by different cell sizes is plotted as function of time.

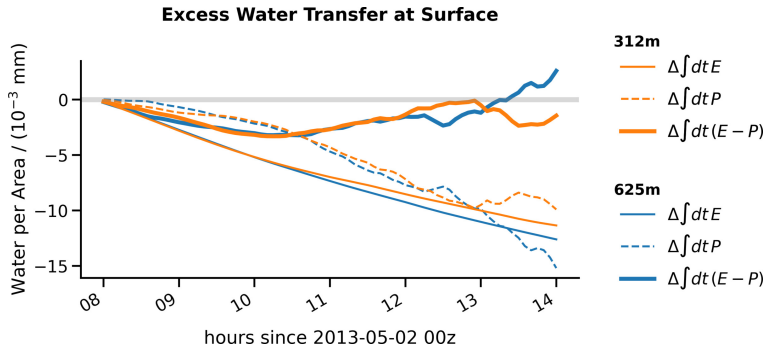

FIGURE 8 Contributions to excess water transfer at the surface. Differences ("absorbing" vs. "scattering") in accumulated precipitation (dashed lines) are compared to differences in accumulated water fluxes from evaporation (thin solid lines) for grid spacings of 312 m (orange) and 625 m (blue). Accumulations start at 8z. The difference between evaporation and precipitation is shown with thick solid lines.